Research Square

Preprints are preliminary reports that have not undergone peer review.
They should not be considered conclusive, used to inform clinical practice,
or referenced by the media as validated information.

Finite-Element-Assisted Design of a Compact SOI Sagnac- Loop Fabry–Pérot Refractive-Index Sensor

Muhammad Ali Butt

ali.butt@pw.edu.pl

Warsaw University of Technology

Bartosz Janaszek

Warsaw University of Technology

Article

Keywords: Silicon-on-insulator, Sagnac loop reflectors, Fabry–Pérot-like resonance, Refractive-index sensing, Integrated photonics

Posted Date: November 24th, 2026

DOI: https://doi.org/10.21203/rs.3.rs-11119529/v1

License: This work is licensed under a Creative Commons Attribution 4.0 International License.
Read Full License

Additional Declarations: No competing interests reported.

Finite-Element-Assisted Design of a Compact SOI Sagnac-Loop Fabry–Pérot Refractive-Index Sensor

Muhammad Ali Butt, Bartosz Janaszek
Warsaw University of Technology, Institute of Microelectronics and Optoelectronics, Koszykowa 75, 00-662, Warsaw, Poland
**Correspondence: ali.butt@pw.edu.pl*

Abstract

This work presents a finite-element-assisted numerical design of a silicon-on-insulator Sagnac-loop-reflector Fabry-Pérot resonator for bulk refractive-index sensing in the O-band. The O-band was selected for its relatively low water absorption compared with wavelengths near 1.4 μm and its compatibility with standard fibre components. Two directional-coupler-based Sagnac loop reflectors form wavelength-dependent mirrors that enclose a central phase-accumulation cavity. The complete device was analysed using a two-dimensional effective-index finite-element model, with a 400 nm wide and 220 nm thick silicon waveguide. Directional-coupler length, coupling gap, cavity length, and the common radius of all curved sections were optimized. The selected geometry comprises an 8 μm common radius, 2 μm coupler interaction length, 80 μm cavity length, and 150 nm coupler gap. A conventional ridge-waveguide connecting cavity (Structure-I) was compared with Structure-II, in which the connecting waveguide incorporates a rectangular-hole subwavelength-grating cavity section having a 220 nm period and a fill factor of 0.50. The 3D modal analysis reveals that the rectangular-hole SWG increases the evanescent-field ratio from approximately 0.079 for the conventional ridge waveguide to 0.458, corresponding to a 5.8-fold enhancement in analyte-accessible optical-power overlap.. For analyte refractive indices ranging from 1.330 to 1.334, Structure-I and Structure-II exhibit sensitivities of 130 and 192 nm/RIU, respectively. At n_a = 1.330, the corresponding full widths at half maximum (FWHMs) are 0.10 and 0.16 nm, yielding loaded quality factors of 1.31×10^4 and 8.20×10^3 and figures of merit (FOMs) of 1300 and 1200 RIU^{-1}, respectively. The incorporation of the rectangular-hole SWG cavity enhances refractive-index sensitivity by approximately 48%, although this improvement is accompanied by resonance broadening and a slight reduction in FOM, highlighting the trade-off between sensitivity and spectral selectivity.

Keywords: Silicon-on-insulator; Sagnac loop reflectors; Fabry–Pérot-like resonance; Refractive-index sensing; Integrated photonics

1. Introduction

Integrated photonic refractive-index sensors have attracted considerable attention for chemical, biological, and environmental analysis because they can convert small variations in the optical properties of an analyte into measurable spectral or intensity changes[1,2]. Silicon-on-insulator technology is particularly attractive for this purpose because of its high refractive-index contrast, compact footprint, mature fabrication processes, and compatibility with large-scale photonic integration[3,4]. In an optical waveguide sensor, a fraction of the guided optical field extends into the surrounding cladding as an evanescent field[5]. Changes in the refractive index of the surrounding medium perturb the effective modal index and accumulated optical phase, enabling label-free sensing through a measurable displacement of an interference fringe or resonance wavelength[6,7].

Resonant and interferometric photonic structures are widely employed to enhance light-matter interaction and improve wavelength-interrogation performance [8,9]. Microring

resonators[8], photonic-crystal cavities[6], Bragg-grating devices[10], Mach–Zehnder interferometers[11], and Fabry–Pérot resonators[12] have all been explored for refractive-index sensing. Among these approaches, Fabry–Pérot cavities are appealing because their spectral response arises from multiple reflections between two optical mirrors separated by a phase-accumulation region[13]. The resonance wavelength, free spectral range, linewidth, and extinction ratio can be tailored through the cavity length, mirror reflectivity, propagation loss, and wavelength-dependent phase response[14]. However, the practical utility of an integrated Fabry–Pérot sensor depends not only on its spectral characteristics but also on fabrication tolerance, device compactness, optical accessibility, and compatibility with surface functionalization and microfluidic delivery.

Sagnac loop reflectors provide a useful route for realizing integrated optical mirrors using only directional couplers and closed waveguide loops[15–17]. An input field entering a Sagnac loop is divided into counterpropagating components by the directional coupler. After circulating around the loop, these components recombine coherently, producing wavelength-dependent transmission and reflection. The effective reflectivity of the loop is governed principally by the coupling condition of the directional coupler, while the loop path determines its phase response[17]. When two Sagnac loop reflectors are connected through an intermediate waveguide, repeated reflections between them establish a compound Fabry-Pérot-like cavity. This architecture provides independent yet coupled control of the cavity phase and reflector properties, making it suitable for systematic optimization of the interference response[13].

Compared with conventional Fabry–Pérot architectures based on Bragg gratings, subwavelength gratings, photonic crystals, or etched discontinuities, a Sagnac-loop-reflector cavity formed from conventional ridge waveguides, curved sections, and directional couplers offers a comparatively straightforward and fabrication-compatible implementation[14,18]. The baseline configuration avoids densely patterned nanoscale features, abrupt refractive-index discontinuities, and highly precise periodic structures, and can potentially be fabricated using a single waveguide-patterning and etching step on a silicon-on-insulator (SOI) platform. The SOI platform provides high refractive-index contrast, strong optical confinement, compact waveguide bends, and compatibility with mature CMOS fabrication processes[3,19]. For appropriately selected dimensions, its 220-nm-thick silicon device layer supports single-mode ridge-waveguide operation in the O-band. The connecting waveguide determines the cavity phase accumulation and free spectral range, while the directional-coupler gaps and interaction lengths govern the splitting ratio, effective Sagnac-mirror reflectivity, resonance linewidth, and extinction ratio. Its continuous waveguide surfaces also facilitate localized upper-cladding removal, surface functionalization, and microfluidic integration. Although dimensional variations in the directional couplers affect the coupling condition and reflector response, the baseline Sagnac-loop cavity is generally less geometrically demanding than photonic-crystal and subwavelength-grating cavities[20].

The sensing response can be further tailored by replacing the connecting ridge-waveguide section with a subwavelength-grating (SWG) waveguide incorporating periodic rectangular apertures [21,22]. This section supports Bloch-mode propagation and increases the accessible waveguide–analyte interface at the hole boundaries. Variations in the surrounding refractive index perturb the Bloch-mode propagation constant and, consequently, the cavity round-trip phase, potentially increasing the resonance-wavelength shift. This potential benefit must, however, be balanced against the additional scattering loss and fabrication sensitivity associated with the periodic geometry[23].

In this work, a compact SOI Sagnac-loop-reflector Fabry–Pérot resonator is numerically investigated for bulk refractive-index sensing in the O-band using a two-dimensional effective-index finite-element model. Structure-I employs the conventional ridge-waveguide connecting cavity, whereas Structure-II uses the rectangular-hole SWG connecting

section. The numerical study first evaluates the role of directional coupling and cavity geometry in establishing the compound Fabry–Pérot response, and then compares the spectral characteristics and sensing performance of the two cavity configurations. The objective is to determine whether the enhanced analyte–field interaction of the SWG cavity improves wavelength sensitivity while retaining a practically useful resonance linewidth and spectral contrast.

2. Device design and numerical model

This section establishes the physical architecture and theoretical framework of the proposed resonator, including the directional-coupler and Sagnac-reflector formulations, and describes the finite-element modelling approach used to quantify its spectral response and refractive-index sensing performance.

2.1. Device architecture and operating principle

The proposed photonic device consists of two Sagnac loop reflectors, denoted SLR_1 and SLR_2, connected by a straight waveguide section, as illustrated in Figure 1 (a). Each reflector is formed by a directional coupler whose two output arms are joined to produce a closed loop. The lower access waveguides provide the input and output ports, whereas the inner branches of the two couplers are joined through the connecting waveguide. The resulting structure therefore provides a continuous optical path from the input port to the output port and, simultaneously, supports counterpropagating fields inside each loop. The device is designed on a SOI platform. The silicon guiding layer has a thickness of 220 nm and is patterned into waveguides with a width of 400 nm, supporting a fundamental TE mode with an effective refractive index of 2.5182 at 1310 nm (see the inset in Figure 1 (b)). The buried silicon dioxide layer provides optical isolation from the silicon substrate. The coupling gap in each directional coupler is 150 nm, and the two loops have an identical radius of 5 μm. The device is designed for the fundamental TE-like mode at 1310 nm. The O-band was deliberately selected rather than chosen for convenience. Because the sensing window exposes the guided mode to the analyte along the entire optical path, absorption in the aqueous cladding places a direct upper bound on the attainable loaded quality factor. The absorption coefficient of liquid water near 1310 nm is approximately an order of magnitude smaller than at 1550 nm [24], which relaxes that bound, since the intrinsic limit of detection scales inversely with the loaded quality factor. The directional-coupler interaction length, L_{dc}, is treated as the principal geometrical control parameter because it determines the relative amplitudes and phases of the through-coupled and cross-coupled fields.

Although SiO_2 is retained outside the active region, the upper oxide is removed above the sensing window. The sensing window extends over both Sagnac loops, the two directional couplers, and the connecting waveguide. The microfluidic chamber therefore exposes the complete optical structure to the analyte. A refractive-index change affects not only the phase accumulated along the connecting waveguide (cavity) but also the propagation constants of both loops and the coupling characteristics of the two directional couplers. At directional coupler 1, the incident TE-like mode is divided into clockwise and counterclockwise components. After propagating around SLR_1, the components return to the coupler and interfere coherently. Part of the recombined field is directed toward SLR_2, whereas the remaining part is reflected toward the input. The same process occurs in SLR_2. Consequently, the two loops operate as wavelength-dependent integrated reflectors. Repeated reflections between them establish a compound Fabry–Pérot-like interference response, with the connecting waveguide acting as the principal phase-accumulation region between the two reflectors. The transmission spectrum is therefore governed by directional coupling, propagation loss, the phases accumulated within both loops, the connecting-waveguide phase,

and multiple reflections between the two Sagnac reflectors. The feasibility of the proposed design depends on propagation losses arising from waveguide scattering and absorption in the surrounding analyte. Previous experimental work has demonstrated propagation losses as low as approximately 2.4 dB/cm in fabricated SOI photonic wires[25], while the wavelength-dependent optical constants of water have been reported in the literature[26]. In the proposed sensing configuration, the effective analyte-related loss additionally depends on the fraction of guided optical power interacting with water. Consequently, the total propagation loss and its influence on cavity linewidth and Q-factor will depend on the fabricated waveguide geometry, modal confinement, and surface roughness. The literature-reported propagation loss should therefore be regarded as a reference value rather than a quantitative estimate for the optimized ridge and SWG geometries, whose actual losses require device-specific characterization.

2.2. Directional-coupler and Sagnac-reflector formulation

For two identical parallel waveguides, the cross-coupled power fraction of each directional coupler is approximated as

$$K = \sin^2(\kappa_c L_{dc}), \tag{1}$$

where κ_c is the coupling coefficient per unit length and L_{dc} is the interaction length. Equation (1) shows that power transfer is periodic with coupling length; consequently, increasing L_{dc} does not produce a monotonic increase in Sagnac reflectivity.

The complex single-pass propagation factor of each Sagnac loop is

$$p = a\exp(-j\phi), \tag{2}$$

where a accounts for single-pass field attenuation and $\phi = \beta L_{loop}$ is the accumulated loop phase, with β denoting the propagation constant and L_{loop} is the optical path length of one Sagnac loop. Using the conventional directional-coupler phase relation, the complex field transmission and reflection coefficients of each Sagnac reflector are

$$t_{SLR} = (t^2 - \kappa^2)p, \tag{3}$$

$$r_{SLR} = 2jt\kappa p, \tag{4}$$

Here t and κ are the through- and cross-coupled field-amplitude coefficients, respectively, satisfying $|t|^2 + |\kappa|^2 = 1$ for an ideal lossless directional coupler. The corresponding power transmittance and reflectance are obtained from the squared magnitudes of these field coefficients. At the nominal 3-dB condition, $|t|^2 = |\kappa|^2 = 0.5$, the direct transmission of an ideal lossless Sagnac reflector is minimized and its reflection is maximized. In the complete device, the optimum condition may deviate from the 50:50 coupling condition because of propagation loss, bend loss, wavelength-dependent coupling, and interference between the two reflectors.

The two wavelength-dependent Sagnac reflectors and the connecting waveguide form a compound Fabry–Pérot-like cavity. Resonances occur when the round-trip propagation phase of the connecting section, together with the reflection phases of both Sagnac loops, satisfies constructive interference. This analytical description is used only to interpret the physical response; quantitative spectra are obtained from the full-wave numerical model.

Figure 1(b) defines the geometrical parameters of the proposed device. A common bending radius, R, is assigned to all curved sections; therefore, the Sagnac-loop radius and the cavity-bend radius are identical, i.e., $R_{loop}=R_b=R$. The directional-coupler gap g also contributes to the physical extent and optical path length of the loops. The cavity comprises a straight section of length L_c, connected through bends of radius R. At each directional coupler, two waveguides of width W, separated by the gap g, interact over the coupling length L_{dc}. Accordingly, L_{dc} and g determine the coupling condition, whereas the common radius R and cavity length L_c govern the propagation path and accumulated optical phase.

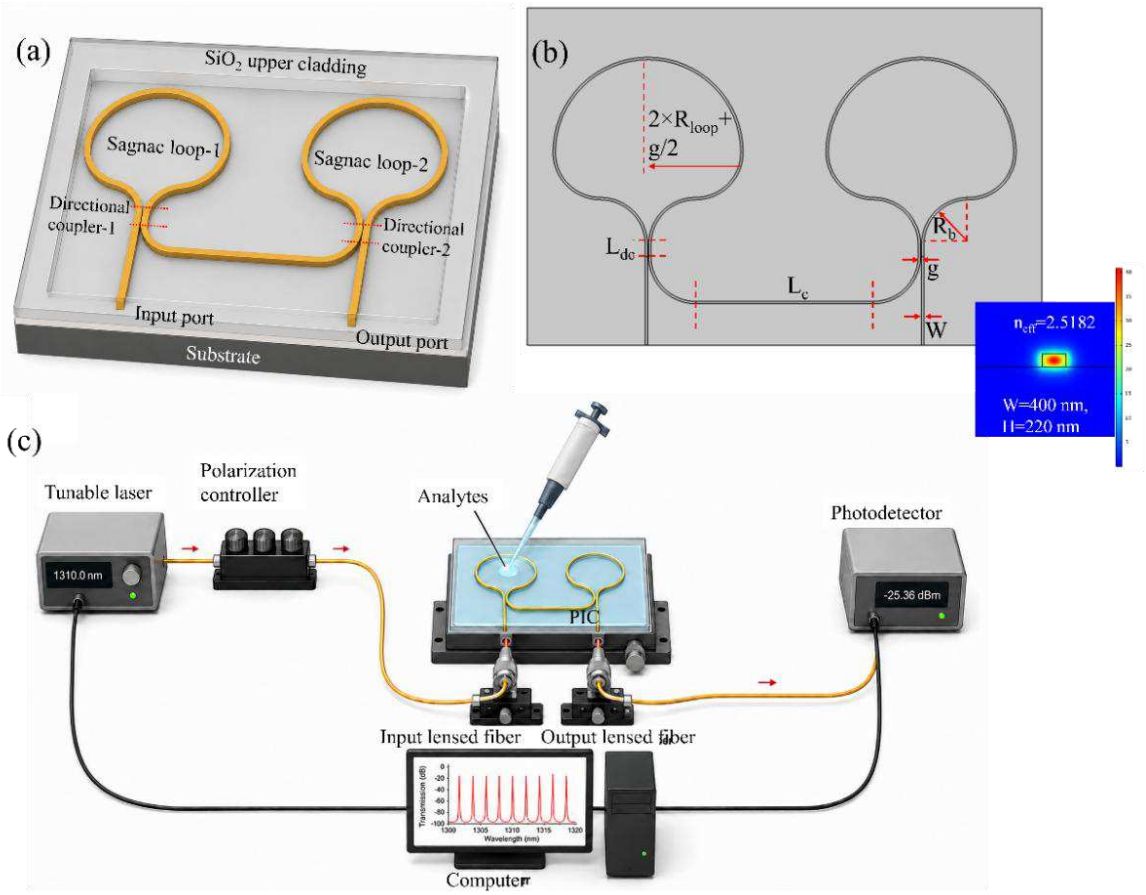

Figure 1. Proposed SOI Sagnac-loop Fabry–Pérot resonator, corresponding to structure-I (a) Three-dimensional device schematic, (b) Two-dimensional layout showing the principal geometrical parameters: R_{loop}, R_b, L_{dc}, L_c, g, and W. The inset shows the effective-index profile of the fundamental TE mode at 1310 nm, (c) Proposed optical characterization setup using a tunable laser, polarization controller, lensed-fiber coupling, microfluidic analyte delivery, photodetector, and computer-based spectral acquisition. Structure-II retains the same Sagnac-loop-reflector configuration but replaces only the central ridge-waveguide cavity with a rectangular-hole SWG section.

2.3. Numerical model

The optical response is calculated in COMSOL Multiphysics 6.4 using the Electromagnetic Waves, Frequency Domain interface, which solves

$$\nabla \times (\mu_r^{-1} \nabla \times \mathrm{E}) - k_0^2 \varepsilon_r \mathrm{E} = 0, \quad (5)$$

where E is the complex electric-field vector, ε_r and μ_r are the relative permittivity and permeability, respectively, and $k_0 = 2\pi/\lambda$ is the free-space wavenumber. All materials are treated as nonmagnetic, such that $\mu_r = 1$.

A two-dimensional in-plane model is used to simulate the complete interferometric structure. Because the vertical confinement of the 220-nm-thick SOI waveguide is not represented explicitly, an effective-index approximation is employed. The effective refractive index, n_{eff}, of the fundamental TE-like mode of the 400 nm × 220 nm silicon waveguide is first obtained from a separate cross-sectional mode analysis at each simulated wavelength and is then assigned to the waveguide domains of the in-plane model.

This reduction converts the original three-dimensional SOI waveguide into an equivalent two-dimensional structure while retaining its modal phase propagation. The approach captures the principal directional-coupling, Sagnac-interference, and multiple-reflection effects with substantially lower computational cost than a complete three-

dimensional wavelength sweep. The fundamental TE-like field is launched at the input waveguide using a harmonic electric-field excitation. Conventional numerical ports are not employed. The input field profile and amplitude are held constant throughout the wavelength, geometry, and refractive-index sweeps. Scattering boundary conditions are applied to the outer boundaries of the computational domain to reduce nonphysical reflections. These boundaries are placed sufficiently far from the device so that they do not perturb the guided or evanescent fields.

For Structure-II, the effective-index approximation represents the vertical confinement, while the 220 nm period and rectangular apertures are explicitly included in the in-plane geometry rather than replaced by a homogenized medium. During sensing simulations, the apertures are assigned the analyte refractive index. The 2D model resolves the in-plane electric-field distribution for the TE-like excitation; the vertical field profile is represented indirectly through the effective index. Therefore, the model does not resolve the complete three-dimensional vector field. Previous studies provide context for this reduced-dimensional approach. Høvik and Aksnes reported that, among the approximations they examined, a full modal solution closely followed 3D results for the photonic components studied [27]. Separately, full-vector 3D-FDTD analysis of SOI subwavelength-grating waveguides demonstrated enhanced analyte interaction and sensing sensitivity[28]. These studies provide context for the modelling approach but do not directly validate the present Sagnac-loop-reflector Fabry–Pérot structure. A full 3D analysis could change the effective index, field overlap, coupler splitting, resonance wavelengths, and free spectral range; out-of-plane effects could also alter linewidth, loaded Q factor, and FOM. The magnitude of these differences for the present device cannot be established from the cited studies alone.

A free triangular mesh was used throughout the in-plane model. The maximum element size was set to 40 nm within the effective-index waveguide domains, including the curved sections and directional-coupler regions, and to 150 nm in the surrounding analyte and other non-guiding domains. The finer discretization in the waveguide domains resolves the guided field distribution and the evanescent coupling across the 150-nm directional-coupler gaps. The wavelength was swept from 1310 to 1318 nm with a step of 0.025 nm. This range lies within the O-band, which is attractive for aqueous-phase SOI sensing because water absorption is lower than near the 1.4-μm absorption band and because mature telecommunication sources, detectors, and fibre components are readily available[29]. For pure water, recommended data give an absorption coefficient of approximately 1.57 cm^{-1} at 1310 nm by interpolation; a direct measurement of distilled water reported 2.36 ± 0.010 cm^{-1}. The recommended value near 1449.3 nm is 32.7 cm^{-1} [30,31]. In addition, operation near 1310 nm is compatible with the low-dispersion window of standard single-mode optical fibre, facilitating future fibre-coupled measurements. A finer local wavelength sweep was performed around selected resonances to accurately determine the FWHM.

For sensing simulations, the analyte was treated as a generic water-based medium with n_a varied from 1.330 to 1.334; no specific dissolved species was assumed. The modified analyte index was assigned uniformly to the entire open sensing region above both loops, both couplers, and the connecting waveguide. The geometrical parameters and the ranges examined in the numerical optimization are summarized in **Table 1**. Unless otherwise stated, one parameter was varied at a time while all remaining geometrical parameters were held at their nominal values. Analyte absorption was not included: the medium was represented by a real-valued refractive index, so the reported FWHM and FOM do not include absorption-induced loss.

Table 1. Geometrical parameters and numerical sweep ranges used in the two-dimensional effective-index finite-element simulations of the SOI Sagnac-loop Fabry–Pérot refractive-index sensor.

Geometric variable	**Explanation**	**Range**
R_{loop}	Loop radius	5,6.5,8 and 10 μm
R_b	Bend radius of Sagnac loops	5,6.5,8 and 10 μm
L_{dc}	Length of direction coupler	2.0, 2.25, 2.5, 2.75, 3.0, 4.0 μm
L_c	Length of cavity	20,30,40,50,60,70,80 μm
W	Width of waveguide	400 nm
H	Height of waveguide	220 nm
a	Width of rectangular hole	200 nm
x	Length of rectangular hole	100-150 nm
y	Gap between two rectangular holes	100-150 nm
FF	Fill factor	y/(x+y)

2.4. Extraction of transmission and performance parameters

Because field excitation rather than numerical ports is used, the response is evaluated using line integrations across identical straight sections of the input and output waveguides. The integrated field amplitudes are defined as

$$A_{\mathrm{in}} = \int_{\Gamma_{\mathrm{in}}} E_{\mathrm{t}}\, \mathrm{d}l, \qquad A_{\mathrm{out}} = \int_{\Gamma_{\mathrm{out}}} E_{\mathrm{t}}\, \mathrm{d}l, \tag{6}$$

where E_t is the selected transverse electric-field component and Γ_{in} and Γ_{out} denote the input and output integration boundaries. The transmission is evaluated directly in decibels as

$$T_{\mathrm{dB}} = 10\log_{10}\left(\left|\frac{A_{\mathrm{out}}}{A_{\mathrm{in}}}\right|^2\right). \tag{7}$$

The same excitation normalization and integration-line positions are retained in every simulation. The lines are placed across straight waveguide sections and sufficiently far from the coupling regions to avoid sampling strongly perturbed local fields.

The resonance wavelength, λ_r, is identified from the selected transmission maximum or minimum. The free spectral range is taken as the absolute wavelength separation between two consecutive resonances. The loaded quality factor is calculated from

$$Q = \frac{\lambda_{\mathrm{r}}}{\mathrm{FWHM}}, \tag{8}$$

where FWHM is the full width at half maximum of the selected resonance. The extinction ratio is evaluated as the absolute difference between the maximum and minimum transmission levels in decibels.

2.5. Geometrical optimization and sensing model

The directional-coupler length is swept from 2 to 4 μm while the 150-nm coupling gap and all other geometrical parameters are held constant. For every value of L_{dc}, the resonance wavelength, FSR, FWHM, quality factor, extinction ratio, and insertion loss are extracted. The configuration around $L_{\mathrm{dc}} = 2$ μm produces pronounced interference fringes, indicating sufficient effective reflection from the two Sagnac loops to establish a compound cavity. When L_{dc} is increased toward approximately 3–4 μm, the fringes become weak or disappear. This behavior is attributed primarily to the periodic power-transfer characteristic of the directional coupler and the associated change in Sagnac reflection, rather than to an automatic increase in propagation loss.

Figure 2 summarizes the numerical optimization of the proposed Sagnac-loop-reflector Fabry–Pérot (FP) cavity. The effects of directional-coupler length L_{dc}, cavity length L_c, directional-coupler gap g, and loop radius R on the transmission response were systematically evaluated. Figure 2(a) shows that the directional-coupler length L_{dc} strongly controls the coupling condition of the Sagnac loop reflectors and, consequently, the FP interference contrast. At L_{dc}=2 µm, sharp resonant transmission features are obtained and the transmission minima reach approximately −43 dB. As L_{dc} increases to 2.25 and 2.5 µm, the resonances become less pronounced and the minimum transmission rises to approximately −32 and −22 dB, respectively. For L_{dc}=3 and 4 µm, the spectrum shifts towards higher transmission levels, with maxima of about −3 and −2 dB, respectively; however, the FP modulation is substantially weakened. This behaviour results from the change in directional-coupler power splitting, which alters the effective reflectivity of the Sagnac loop reflectors and the fraction of light coupled into the cavity. Therefore, L_{dc}=2 µm was selected to retain strong cavity excitation and high-contrast resonances.

The influence of the connecting-waveguide length L_c is presented in Figure 2(b). Increasing L_c from 20 to 80 µm increases the optical length of the FP cavity, resulting in a reduced FSR. For L_c=20 µm, the separation between neighbouring resonances is approximately 3.2 nm. With increasing cavity length, additional FP modes appear within the same spectral range, and the resonance spacing decreases to approximately 2 nm for L_c=80 µm. Thus, the connecting waveguide provides direct control over the spectral periodicity while maintaining the compact footprint of the loop reflectors. The spectra in Figure 2(b) are vertically offset for clarity.

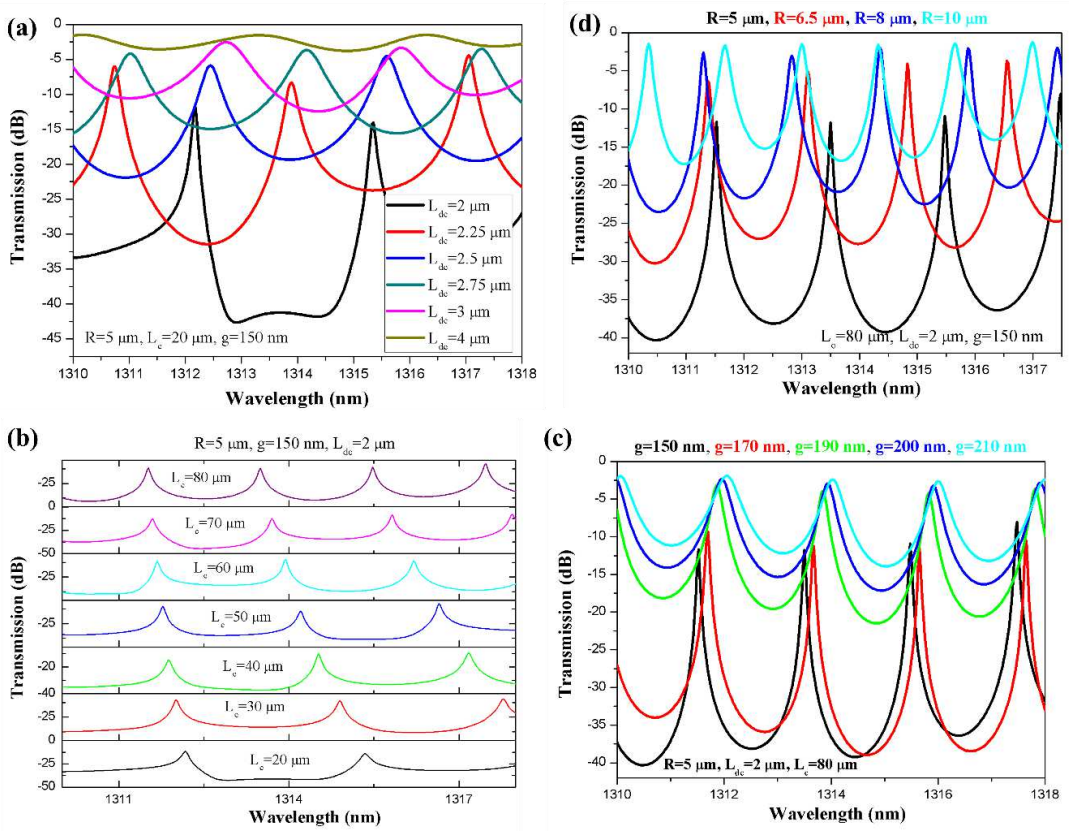

Figure 2. Simulated transmission spectra of the proposed photonic device during geometric optimization: (a) directional-coupler length L_{dc}, varied from 2 to 4 µm; (b) connecting-waveguide length L_c, varied from 20 to 80 µm; (c) directional-coupler gap g, varied from 150 to 210 nm; (d) loop radius R, varied from 5 to 10 µm.

Figure 2(c) illustrates the effect of directional-coupler gap (g). The smallest gap, g=150 nm, produces strong evanescent coupling and sharp FP resonances, with transmission minima close to −40 dB. Increasing the gap to 170 nm maintains the narrow spectral response but modifies the resonance contrast. At larger gaps of 190, 200, and 210 nm, the spectral resonances become progressively broader and shallower, while the transmission minima increase to approximately −20, −17, and −14 dB, respectively. Although the higher transmission level at larger gaps indicates reduced attenuation at the output, it is accompanied by weaker cavity excitation and lower FP modulation. Therefore, g=150 nm was selected to ensure sufficiently strong coupling and well-defined resonant interference.

Finally, Figure 2(d) shows the effect of loop radius. Increasing R from 5 to 10 μm increases the optical path length and reduces the FSR from approximately 2 nm for R=5 μm to approximately 1.4 nm for R=10 μm. The overall transmission level increases with radius. In particular, the resonant maxima increase from around −12 dB for R=5 μm to nearly −1.5 dB for R=10 μm, indicating reduced loss in the larger loops. This improvement is mainly attributed to lower bend-induced radiation loss, which increases the effective reflectivity of the practical Sagnac loop reflectors by reducing propagation attenuation within the loops. Nevertheless, the R=5 μm case exhibits the deepest modulation, with minima close to −40 dB, whereas the R=10 μm design exhibits lower loss but weaker contrast. A radius of R=8 μm was therefore selected as a compromise between compactness, transmission level, spectral contrast, and FSR. Taken together, L_{dc} and g determine the feedback provided by the Sagnac reflectors, while L_c and R influence the cavity phase, FSR, and bend-related loss. The selected combination is the preferred compromise within the parameter ranges tested; the results do not establish it as a unique or global optimum.

Based on this optimization, the final device geometry was chosen as R=8 μm, L_{dc}=2 μm, L_c =80 μm, and g=150 nm. For the optimized devices, the linewidth was evaluated at the nominal analyte refractive index of n_a=1.33. The simulated transmission expressed in decibels was converted to linear power using $T_{lin} = 10^{\frac{T_{dB}}{10}}$. For each selected resonance, the local baseline transmission T_{min} and peak transmission T_{max} were identified using Origin software. The FWHM was then determined from the wavelength separation at the half-height level, $T_{1/2}=T_{min}+(T_{max}-T_{min})/2$.

2.6. Possible realization of experimental characterization

Although the present study is numerical, the proposed device can be experimentally characterized using the arrangement shown in Figure 1(c). A tunable laser covering 1310–1318 nm would be connected to a polarization controller to excite the fundamental TE-like mode. Light would be coupled into and collected from the chip using aligned lensed fibers, while the transmitted optical power would be sampled with a photodetector during the wavelength sweep. A reference spectrum obtained without the sensing structure, or with a reference waveguide, would be used to normalize the measured transmission and reduce the influence of fiber-to-chip coupling losses. The sensing response would be characterized by introducing the analyte into the exposed region and recording the wavelength-dependent transmission. Variations in the analyte refractive index modify the effective modal index and accumulated optical phase, resulting in a measurable displacement of the interference resonances.

The sensing window shown in Figure 1(a) extends over the complete resonator, including both Sagnac loop reflectors, both directional couplers, and the connecting cavity. The analyte can be delivered through a microfluidic channel positioned over this window, allowing it to cover all exposed sections of the structure, including the rectangular apertures in Structure-II. After measurement, the channel can be removed, and the chip cleaned with acetone followed by isopropanol. The simulations assume complete analyte infiltration into the apertures; this can be checked experimentally.

3. Results and discussion

3.1. Three-dimensional modal characterization of the ridge and rectangular-hole SWG waveguide

Three-dimensional (3D) numerical analysis was performed using the Electromagnetic Waves, Frequency Domain (EWFD) interface in COMSOL Multiphysics 6.4 to investigate the modal characteristics of the conventional ridge and rectangular-hole SWG waveguides. Unlike the two-dimensional effective-index approximation employed for the complete Sagnac-loop Fabry–Pérot resonator, the 3D models explicitly resolve the silicon waveguide cross-section and surrounding dielectric regions. The waveguide thickness was fixed at 220 nm, and the optical response was investigated over the wavelength range of 1300–1330 nm. Finite-length waveguides were excited through input and output ports, with scattering boundary conditions applied to the exterior computational boundaries. The optical confinement factor and evanescent-field ratio (EFR) were evaluated from the longitudinal component of the time-averaged Poynting vector, integrated over the silicon and analyte-accessible regions, respectively, and normalized to the total guided power. For the periodic SWG structure, cells adjacent to the ports were excluded from the power integrations to minimize end effects.

3.1.1. Ridge waveguide

Figure 3 presents the modal characteristics of the conventional silicon ridge waveguide for widths (W) ranging from 350 to 400 nm in increments of 10 nm. As shown in Figure 3(a), the optical confinement factor increases with waveguide width and decreases slightly with wavelength. For W = 400 nm, the confinement factor decreases from approximately 0.855 at 1300 nm to 0.845 at 1330 nm. Conversely, Figure 3(b) shows that the EFR decreases with increasing width but increases with wavelength. For W = 400 nm, the EFR varies from approximately 0.078 to 0.083, indicating limited optical-power overlap with the surrounding analyte. The simulated electric-field distribution at 1310 nm (Figure 3(c)) further illustrates strong field localization within the silicon core. The smooth variation of confinement and EFR across the investigated widths indicates a gradual modal response to geometrical changes, suggesting that moderate width deviations modify the analyte interaction without causing abrupt changes in the calculated modal characteristics.

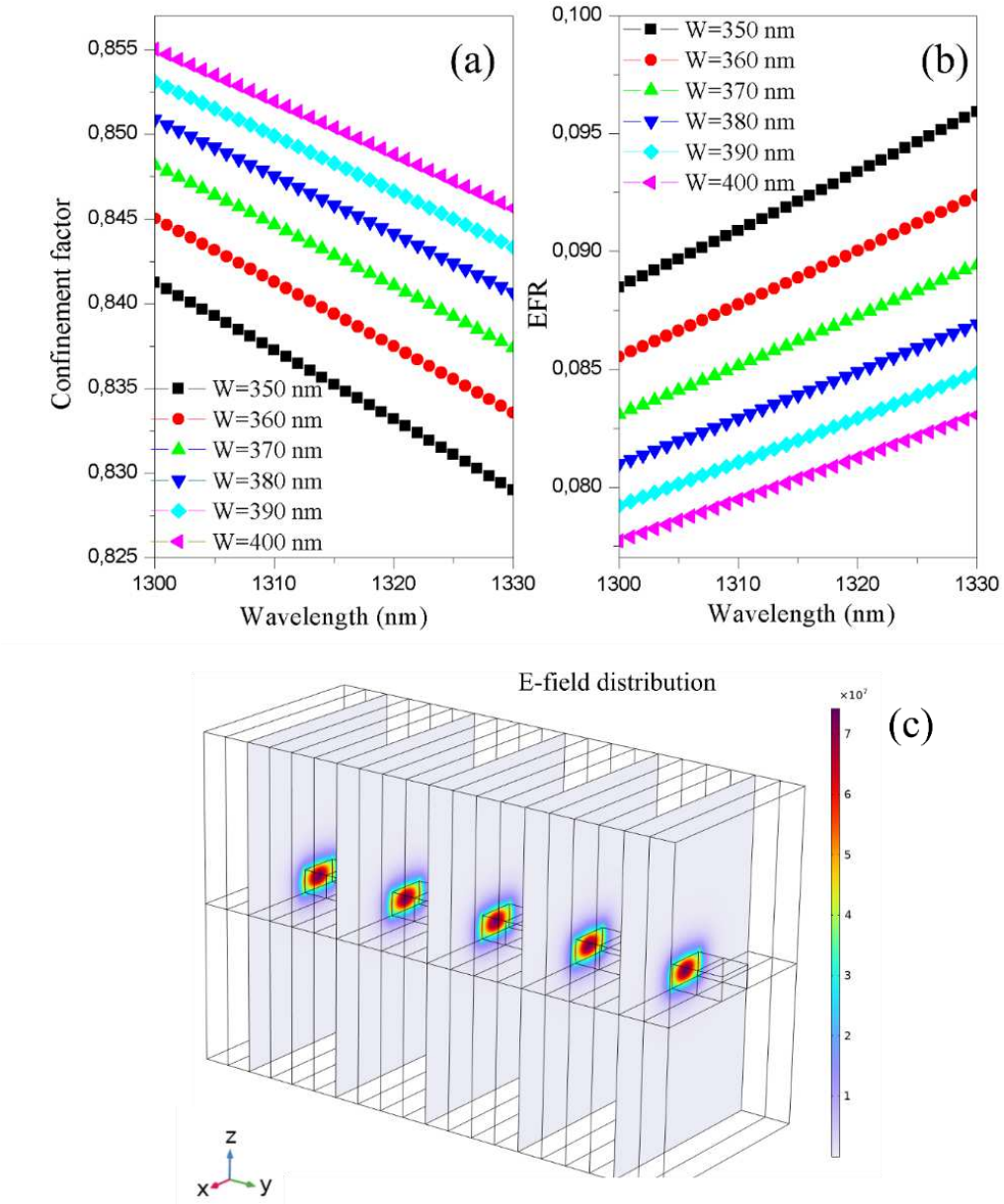

Figure 3. Three-dimensional modal characterization of the conventional silicon ridge waveguide with a fixed thickness of 220 nm and widths ranging from 350 to 400 nm. (a) Optical confinement factor and (b) EFR as functions of wavelength; (c) simulated electric-field magnitude at 1310 nm for W = 400 nm, illustrating optical-field confinement within the silicon core and penetration into the surrounding medium.

3.1.2. Rectangular-hole SWG waveguide

Figure 4 presents the 3D numerical characterization of the rectangular-hole SWG waveguide with a width of W = 400 nm and rectangular-aperture width of a = 200 nm. The grating period (Λ) was varied from 200 to 250 nm in increments of 10 nm, while the fill factor was maintained at FF = 0.5. Figure 4(a) shows that the optical confinement factor generally decreases with increasing wavelength, varying from approximately 0.427–0.432 at 1300 nm to 0.417–0.422 at 1330 nm. Conversely, the EFR in Figure 4(b) generally increases with wavelength, ranging from approximately 0.456 to 0.463. These variations indicate wavelength- and geometry-dependent redistribution of guided optical power between the silicon and analyte-accessible regions. For the selected Λ = 220 nm configuration, the confinement factor remains approximately 0.420–0.428, while the EFR varies from approximately 0.457 to 0.460.

Figure 4(c) presents the normalized transmission spectra, revealing a stronger dependence on grating period and wavelength than the confinement factor and EFR. While certain configurations exhibit pronounced transmission minima, the selected Λ = 220 nm waveguide maintains transmission across the investigated spectral range without a pronounced stopband-like attenuation feature. Figures 4(d) and 4(e) illustrate the two-dimensional and three-dimensional representations of the simulated optical-field distribution at 1310 nm for the selected SWG configuration (Λ = 220 nm, FF = 0.5), respectively. The field exhibits periodic modulation along the propagation direction, consistent with guided Bloch-mode behavior, while extending into the rectangular apertures and surrounding analyte region. These distributions illustrate the spatial characteristics of the guided mode and support the enhanced analyte-field interaction indicated by the calculated EFR.

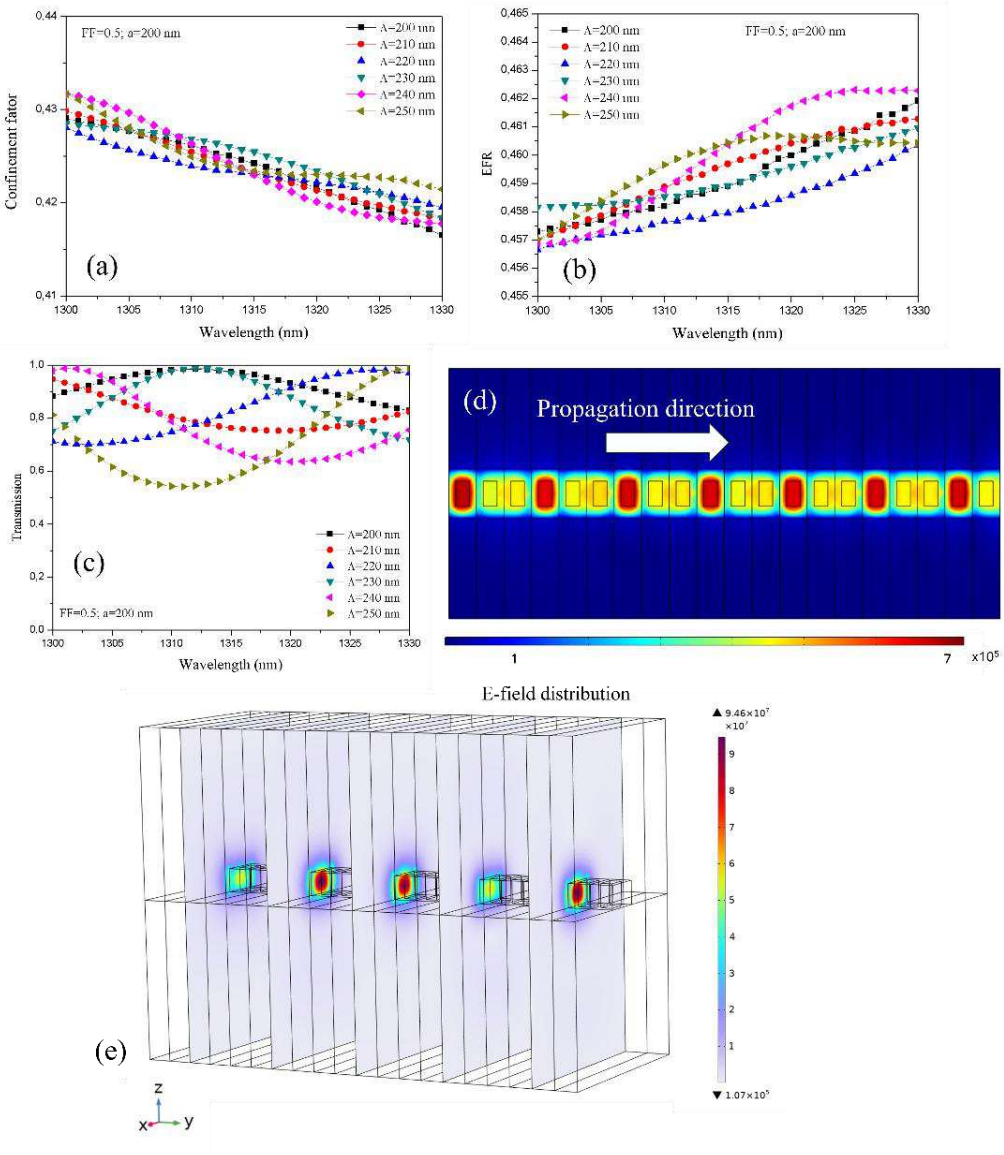

Figure 4. Three-dimensional numerical characterization of the rectangular-hole SWG waveguide (W = 400 nm, thickness = 220 nm, a = 200 nm, FF = 0.5) for grating periods Λ = 200–250 nm. (a) Optical confinement factor, (b) evanescent-field ratio (EFR), and (c) normalized transmission as functions of wavelength; (d) two-dimensional magnetic-field magnitude distribution and (e) three-dimensional electric-field magnitude distribution at 1310 nm for Λ = 220 nm, illustrating periodic field modulation and penetration into the rectangular apertures.

3.1.3. Comparative analysis and fabrication considerations

The 3D simulations reveal distinct modal characteristics for the conventional ridge and rectangular-hole SWG waveguides, as summarized in Figure 5. At 1310 nm, the ridge waveguide (W = 400 nm) exhibits a confinement factor of approximately 0.85 and an EFR of 0.079, compared with 0.42 and 0.458, respectively, for the SWG waveguide (Λ = 220 nm, FF = 0.5). The approximately 5.8-fold increase in EFR is associated with reduced silicon-core confinement and increased optical-power overlap with the analyte-accessible regions introduced by the rectangular apertures. This enhanced interaction is consistent with the higher refractive-index sensitivity of Structure II (192 nm/RIU) compared with Structure I (130 nm/RIU), representing an improvement of approximately 47.7%. The difference between the relative EFR and sensitivity enhancements reflects the dependence of the resonance shift on the optical response of the complete Sagnac-loop Fabry–Pérot structure.

The geometrical sweeps also provide insight into fabrication-related variations. The ridge waveguide exhibits gradual changes in confinement and EFR with width, whereas the SWG shows relatively modest variations in these parameters with grating period but more pronounced changes in transmission. This indicates that periodic-geometry deviations may affect optical throughput even when modal overlap remains relatively stable. Consequently, accurate control of the SWG period, fill factor, and aperture dimensions is important for reproducible device performance. However, quantitative fabrication tolerances require further investigation of dimensional deviations and associated scattering losses.

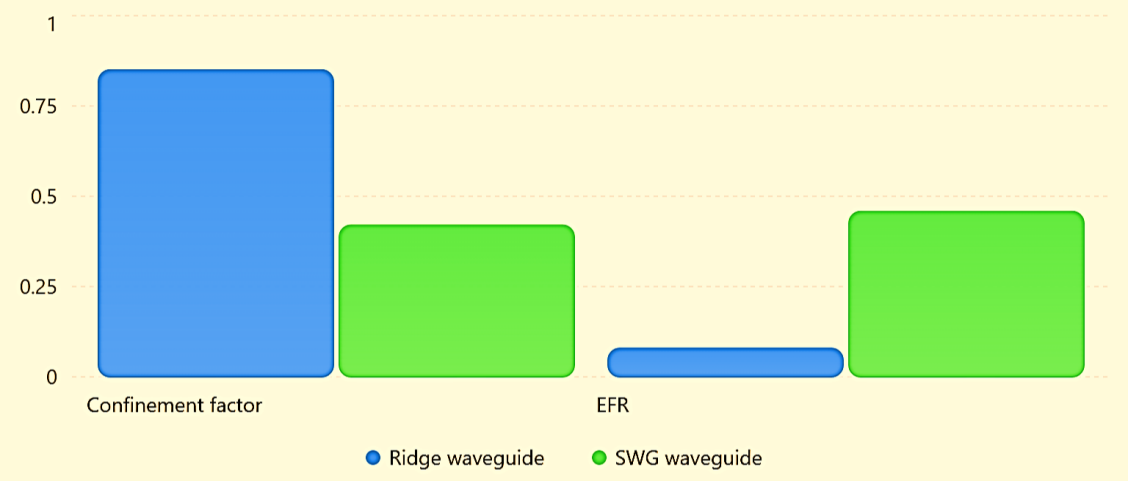

Figure 5. Comparison of the optical confinement factor and evanescent-field ratio (EFR) for conventional ridge and rectangular-hole SWG waveguides at 1310 nm. Both waveguides have W = 400 nm and a silicon thickness of 220 nm. The SWG configuration employs Λ = 220 nm, FF = 0.5, and a rectangular-aperture width of 200 nm.

3.2. Refractive index sensing

The refractive-index sensitivity is determined from the displacement of a selected resonance as the analyte index changes[32]:

$$S = \frac{\Delta\lambda_{\mathrm{r}}}{\Delta n_{\mathrm{a}}}; \tag{9}$$

where S is expressed in nm/RIU. The slope of a linear fit to λ_{r} as a function of n_{a} is used when more than two refractive-index values are simulated. The sensing figure of merit is

$$\mathrm{FOM} = \frac{S}{\mathrm{FWHM}}\,[33]; \tag{10}$$

The optimized geometry is selected by considering sensitivity, linewidth, quality factor, extinction ratio, insertion loss, and spectral readability simultaneously rather than maximizing the wavelength shift alone. The spectral response originates from the dependence of the Fabry–Pérot resonance condition on the effective propagation constant of the cavity mode. A resonance is established when the round-trip phase accumulated between the two Sagnac-loop mirrors satisfies the phase-matching condition. When the ambient refractive index increases, the evanescent field extending from the waveguide into the surrounding medium experiences a higher refractive index. This increases the mode effective index, increases the accumulated cavity phase at a fixed wavelength, and shifts the resonance to a longer wavelength to restore the resonance condition. The resulting red shift is therefore the basis of bulk refractive-index sensing.

Figures 6(a) and 6(b) show that this red shift occurs systematically for both structures as the ambient refractive index increases from 1.330 to 1.334. Although the device response was evaluated over the full 1310–1318 nm interval, the sensing analysis is presented over the narrower 1310–1313 nm window because it contains the selected resonances and allows their refractive-index-induced shifts to be resolved clearly. The selected refractive-index interval represents a near-aqueous bulk-sensing regime relevant to variations in dissolved-solute concentration or total biomolecular content; it is not intended to emulate the response to a single dilute biomarker, for which surface functionalization together with a local binding-layer model would be required[34]. The extracted resonance shifts, summarized in Figure 6(c), exhibit an approximately linear dependence on ambient refractive index over the investigated range. Structure-I provides a sensitivity of 130 nm/RIU, whereas Structure-II reaches 192 nm/RIU.

The higher sensitivity of Structure-II is attributed to the rectangular-hole SWG section, which increases the interaction between the guided optical field and the surrounding analyte. The periodic apertures, assumed to be fully infiltrated by the aqueous analyte, introduce additional analyte-accessible interfaces and modify the propagation characteristics of the guided mode. Consequently, changes in analyte refractive index produce a greater perturbation of the accumulated cavity phase, resulting in an approximately 48% sensitivity enhancement relative to Structure-I.

The linewidth analysis was performed at the nominal analyte refractive index of n_a=1.330. Structure-I exhibits a resonance wavelength of 1311.3 nm and an FWHM of 0.10 nm, resulting in a simulated loaded quality factor of 1.31×10^4. Structure-II exhibits a resonance wavelength of 1310.5 nm and an FWHM of 0.16 nm, corresponding to a simulated loaded quality factor of 8.20×10^3. Using the figure-of-merit definition above, the corresponding FOM values are 1300 RIU^{-1} for Structure-I and 1200 RIU^{-1} for Structure-II.

Although the enhanced analyte-field interaction identified in Section 3.1.3 is consistent with the higher sensitivity of Structure-II, the improvement is accompanied by a 60% increase in FWHM, reducing the loaded Q factor by approximately 37% and the FOM by about 8%. These results demonstrate that increased analyte interaction does not necessarily improve linewidth-normalized sensing performance. Structure-II offers greater wavelength sensitivity, whereas Structure-I retains narrower resonances and a slightly higher FOM. The preferred configuration therefore depends on the intended interrogation conditions and the balance between sensitivity and spectral linewidth.

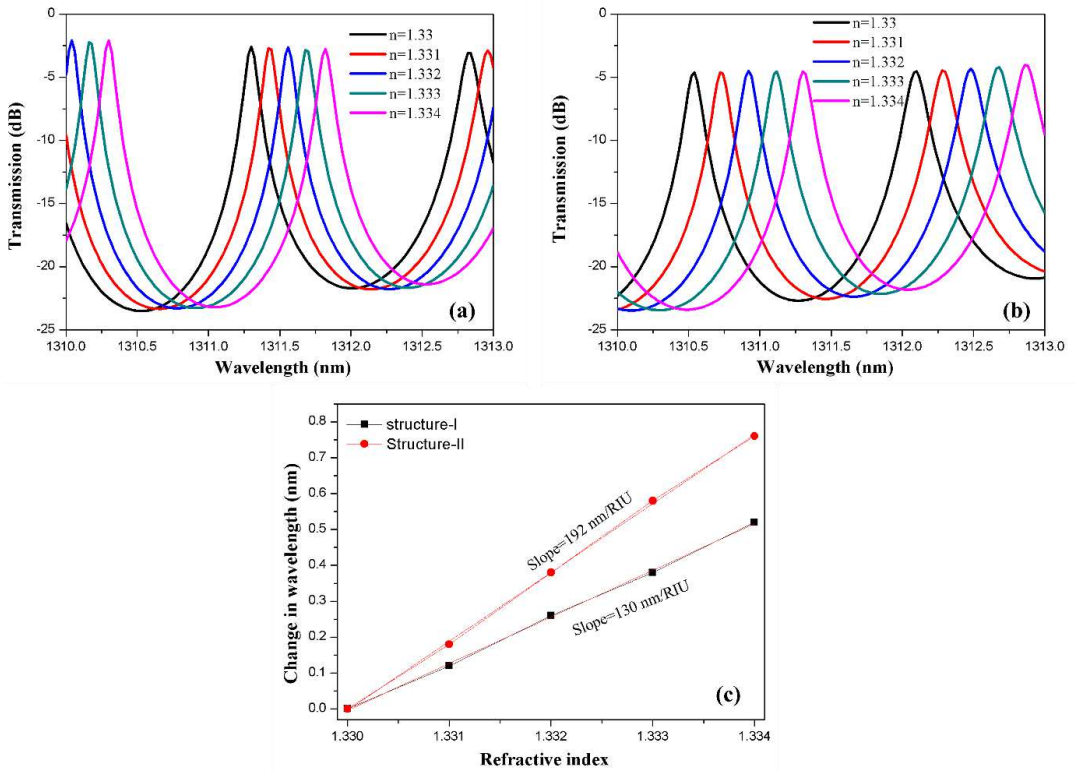

Figure 6. Simulated transmission spectra of (a) Structure-I and (b) Structure-II for surrounding refractive indices ranging from 1.330 to 1.334. (c) Resonance-wavelength shift as a function of refractive index for both structures, yielding sensitivities of 130 nm/RIU for Structure-I and 192 nm/RIU for Structure-II.

The reported FWHM and FOM values were obtained without explicitly modelling sidewall-roughness-induced scattering. They therefore describe the simulated response of the nominal structures and should not be interpreted as predictions of fabricated-device performance. Sidewall scattering would add intrinsic cavity loss, broaden the resonances, and reduce the loaded Q factor and FOM; its magnitude may differ between the ridge and SWG structures because their etched interfaces differ. Without roughness data for the fabrication process, this difference cannot be quantified, and the comparison is limited to the loss mechanisms represented in the present model. The reported FOM values therefore rank Structure-I higher than Structure-II for the modelled geometries, but process-dependent sidewall roughness may change the magnitude of this difference.

3.3. E-field distribution plots

Figure 7 presents the simulated electric-field distributions of Structure-II at two wavelengths. In Figure 7(a), at λ=1311.3 nm, the field distribution indicates weak excitation of the Fabry-Perot cavity (FPC) mode. The field is mainly confined within the left Sagnac-loop region, while the connecting SWG cavity section and the second loop show only weak excitation. This behavior is consistent with an unfavorable round-trip phase condition for resonant field enhancement within the cavity. In contrast, Figure 7(b) shows the field distribution at λ = 1310.5 nm, where pronounced cavity excitation is observed. A strong field extends through the connecting cavity and couples to both Sagnac loops, consistent with resonant interference and enhanced optical-field buildup within the complete device. The inset further shows the periodic electric-field modulation in the rectangular-hole subwavelength-

grating (SWG) section, arising from the periodic modulation of the waveguide geometry and its effective optical properties. The enhanced field interaction with the analyte-accessible regions of the SWG provides a physical explanation consistent with the higher refractive-index sensitivity observed for Structure-II.

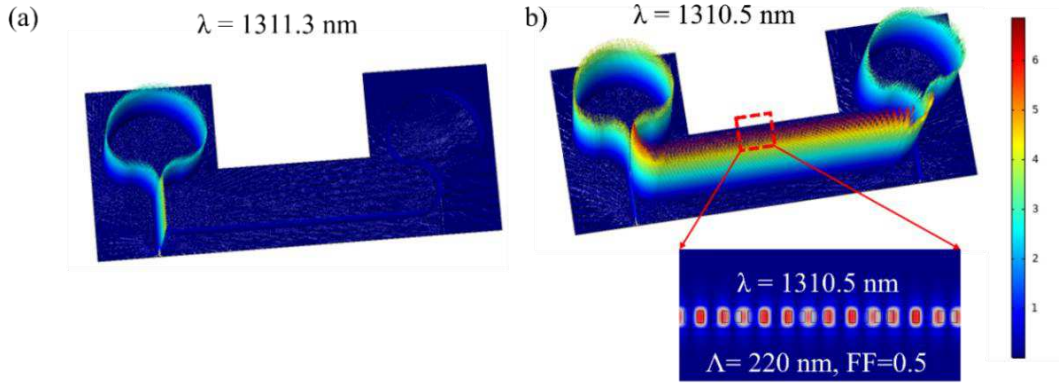

Figure 7. Simulated electric-field distributions of Structure-II at (a) λ=1311.5 nm, where no FPC mode is excited, and (b) λ=1310.5 nm, corresponding to excitation of the FPC mode. The inset shows the field modulation in the rectangular-hole Bragg-grating section. An animated GIF showing the wavelength-dependent evolution of the electric-field distribution is provided in the Supplementary Material.

4. Benchmarking the proposed SLR structure vs. existing sensors

Table 2 compares the proposed Sagnac-loop-reflector Fabry–Pérot sensors with representative integrated resonant refractive-index sensors based on coupled-resonator, Bragg-grating, photonic-crystal, and microring architectures. Since the reported devices operate at different wavelength bands and may differ in sensing configuration, analyte exposure, and loss assumptions, the comparison is intended to identify architectural trade-offs rather than establish an absolute performance ranking.

The conventional Sagnac-loop-reflector Fabry–Pérot design achieves a sensitivity of 130 nm/RIU, a quality factor of 1.31×10^4, and a figure of merit of 1300 RIU^{-1}. Incorporating the rectangular-hole SWG cavity increases the sensitivity to 192 nm/RIU (+48%) while reducing the quality factor to 8.20×10^3 (−37%), so that the FOM is essentially preserved at 1200 RIU^{-1} (−8%). The two configurations are therefore not ordered by merit but are suited to different interrogation regimes, i.e., where the spectral resolution of the interrogator is the limiting factor, the detection limit scales inversely with sensitivity and the SWG variant is preferable, whereas under linewidth- and noise-limited readout the FOM governs and the conventional design retains a marginal advantage. Relative to the CROW structures reported in [35], the conventional Sagnac-loop-reflector Fabry–Pérot provides a 2.2–5.0-fold higher figure of merit at comparable wavelength sensitivity. This result indicates that the improvement arises predominantly from resonance sharpening rather than from a major increase in light–analyte overlap. Its Q-factor also exceeds that of the multi-box sub-wavelength phase-shifted Bragg grating in [36] by 64% and is 1.7–3.4 times higher than those of the CROW devices in [35]. Compared with the O-band Si_3N_4 microring included in Table 2 [37], the conventional Sagnac-loop-reflector Fabry–Pérot provides a 2.6-fold higher quality factor and a 1.6-fold higher FOM. Among the devices listed in Table 2, the conventional Sagnac-loop-reflector Fabry–Pérot has the highest Q-factor among those that are neither travelling-wave resonators nor photonic-crystal cavities.

This response follows from the division of functions within the Sagnac-loop-reflector Fabry–Pérot architecture. The central cavity length primarily determines the free spectral range and sensing interaction length, whereas the Sagnac-loop reflectors provide cavity feedback.

Their reflectivity is governed mainly by the directional-coupler splitting ratio, together with the loop phase and propagation loss. The linewidth can therefore be tailored through the reflector design without requiring a proportional increase in cavity length, while the exposed cavity section can be extended to increase light–analyte interaction without imposing the same change in mirror feedback. In travelling-wave microring resonators, by comparison, the cavity length, interaction length, bend loss, and bus–ring coupling are more strongly interrelated. This separation accounts quantitatively for the position of the present device in Table 2, i.e., a quality factor in the 10^4 range is obtained at a comparatively modest sensitivity of 130 nm/RIU, whereas the high-sensitivity entries [36,38,39] achieve their figures of merit by enlarging the field fraction accessible to the analyte through slot, multi-box or sub-wavelength engineering, and consequently inherit the scattering losses associated with those geometries as well as higher fabrication complexity.

A further distinction concerns the nature of the feedback elements themselves. The Sagnac-loop-reflector Fabry–Pérot does not rely on a Bragg stop band to provide cavity feedback. Consequently, unlike a Bragg-mirror Fabry–Pérot sensor, its resonance is not constrained by displacement relative to a narrow reflection band when the surrounding refractive index changes. Variations in directional-coupler geometry modify the effective Sagnac-reflector response and may affect both the cavity finesse and resonance wavelengths through changes in coupling amplitude and phase. This behavior differs from that of architectures in which the operating point depends on a coupling condition held within narrow tolerances, such as the critically coupled double-loop resonator [38], where the supermode that produces the reported linewidth requires a specific mutual coupling between the two cavities. In the present structure, the corresponding degree of freedom enters as a smooth variation of finesse rather than as a threshold.

Higher FOMs have been reported using critically coupled double-loop resonators[38], microring resonators[40], photonic-crystal cavities[41],[39], and sub-wavelength Bragg-grating engineering[36]. These approaches can provide stronger field confinement or narrower resonances, but commonly require tighter control of coupling conditions or nanometre-scale structural features. In the conventional configuration reported here, the resonator contains no sub-wavelength critical dimensions and no critically coupled resonator pair; the smallest feature is the directional-coupler gap, and the SWG section is introduced only in the second configuration, where it is adopted deliberately in exchange for sensitivity. Operation in the O-band contributes independently to this balance, i.e., absorption by aqueous analytes near 1310 nm is approximately an order of magnitude lower than at 1550 nm, thereby relaxing the cladding-loss ceiling on the loaded quality factor. The same effect has been isolated experimentally on a single chip [37], where moving from the TE mode at 1550 nm to the TM mode at 1310 nm raised the measured quality factor by 93% and reduced the intrinsic limit of detection by 65%. To the best of our knowledge, the Sagnac-loop-reflector Fabry–Pérot resonator has not previously been employed as an integrated refractive-index transducer, nor has any Sagnac-loop device been reported in the O-band. The proposed Sagnac-loop-reflector Fabry–Pérot instead offers a compact resonator in which cavity phase and reflector feedback are separately adjustable, providing a balanced route to linewidth control and refractive-index sensing.

Table 2. Performance benchmarking of the proposed Sagnac-loop-reflector Fabry–Pérot refractive-index sensors against reported resonant integrated photonic sensors based on coupled-resonator, Bragg-grating, photonic-crystal, and microring architectures operating in the O- and C-bands. CROW, coupled-resonator optical waveguide; PSBG, phase-shifted Bragg grating.

Structure	Spectral band	Material platform	Sensitivity (nm/RIU)	Q-factor	FOM (RIU^{-1})	Reference
CROW	C-band	SOI	106.4–120	3.8×10^3–7.8×10^3	261–604	[35]
CROW with SWG feedback	C-band	SOI	185.8–212.2	1.9×10^3–3.8×10^3	228–520	[35]
Coherent cavity with double loop	O-band	SOI	304.02	2.2×10^4	5106	[38]
Multi-box sub-wavelength PSBG	C-band	SOI	579.2	8.0×10^3	2989	[36]
Integrated 2D photonic-crystal microcavity	C-band	SOI	200	4.0×10^2	52	[42]
1D PhC width-modulated stack mode-gap cavity	C-band	SOI	269	2.7×10^4	4686	[41]
Slotted width-modulated 1D photonic crystal stack	C-band	SOI	410	1×10^4	2645	[39]
SOI microring resonator	C-band	SOI	120	1×10^5	7742	[40]
Si_3N_4 microring, TM mode	O-band	Si_3N_4	210.2	4.97×10^3	797	[37]
Sagnac-loop-reflector Fabry–Pérot	O-band	SOI	130	1.31×10^4	1300	This work
Sagnac-loop-reflector Fabry–Pérot with rectangular-hole SWG	O-band	SOI	192	8.20×10^3	1200	This work

5. Conclusion

This numerical study investigates a Sagnac-loop-reflector Fabry–Pérot resonator for refractive-index sensing in the O-band, where integrated refractometric sensing remains less extensively explored than in the C-band. The resonant response arises from round-trip phase accumulation in the connecting cavity, whereas the Sagnac loop reflectors provide the optical feedback that determines the resonance contrast and finesse. The geometrical analysis shows that sensing performance cannot be evaluated from resonance displacement alone; directional coupling, cavity loss, linewidth, and spectral contrast collectively determine the suitability of the device for wavelength-interrogation measurements.

Replacing the ridge-waveguide cavity of Structure-I with a rectangular-hole subwavelength-grating (SWG) section in Structure-II increases the interaction of the cavity mode with the external analyte. The periodic geometry supports an analyte-sensitive Bloch-mode response and increases the optical-field overlap with the aqueous medium, including at the hole boundaries. Consequently, Structure-II increases the wavelength sensitivity by approximately 48%, from 130 to 192 nm/RIU. This improvement is accompanied by linewidth

broadening from 0.100 to 0.160 nm, resulting in a slightly lower figure of merit. The two configurations should therefore be regarded as complementary rather than universally ranked: Structure-II is advantageous when the wavelength resolution of the interrogator is the principal limitation, whereas Structure-I is preferable when a narrower resonance and linewidth-normalized sensing performance are the primary requirements. This distinction provides a practical basis for selecting the cavity configuration according to the intended interrogation scheme.

Because the present work is purely numerical, subsequent investigation should assess the tolerance of the SWG geometry to lithographic and etching variations and quantify the influence of realistic propagation and scattering losses. Experimental characterization of fabricated devices would establish whether the predicted sensitivity–linewidth trade-off is retained in practice. For target-specific biochemical sensing, selective surface functionalization, controlled microfluidic delivery, temperature stabilisation, and an on-chip reference channel could subsequently be incorporated.

Acknowledgement

The authors acknowledge the constant support of Warsaw University of Technology in the completion of this work.

Declarations

Disclosures

The authors declare no conflicts of interest.

Ethical Approval

This study did not involve human participants, live vertebrates, or any biological material requiring ethical approval. Therefore, ethical approval was not applicable.

Consent to Participate

Not applicable, as this study did not involve human participants.

Competing interests

N/A

Authors' Contributions: Conceptualization – M.A.B; **Methodology** – M.A.B; **Validation** – B.J. and M.A.B; **Formal Analysis** – M.A.B; **Investigation** – B.J., and M.A.B.; **Writing – Original Draft** – M.A.B. and B.J.; **Writing – Review & Editing** – M.A.B, and B.J.; **Supervision** – M.A.B.

Funding

This research was funded by the National Science Centre, Poland, under the OPUS programme, Grant Agreement No. UMO-2025/59/B/ST7/00052.

Availability of data and materials

The data supporting the findings in this work are available from the corresponding author with a reasonable request.

Consent to Publish

Not applicable, as this study did not involve human participants or identifiable data.

References

1. Butt, M.A.; Imran Akca, B.; Mateos, X. Integrated Photonic Biosensors: Enabling Next-Generation Lab-on-a-Chip Platforms. *Nanomaterials* **2025**, *15*, 731, doi:10.3390/nano15100731.
2. Altug, H.; Oh, S.-H.; Maier, S.A.; Homola, J. Advances and Applications of Nanophotonic Biosensors. *Nat. Nanotechnol.* **2022**, *17*, 5–16, doi:10.1038/s41565-021-01045-5.
3. Al-Qadasi, M.A.; Grist, S.M.; Mitchell, M.; Newton, K.; Kioussis, S.; Chowdhury, S.J.; Randhawa, A.; Liu, Y.; Tisapramotkul, P.; Cheung, K.C.; et al. A Segmented Resonator Architecture for Fixed-Wavelength Silicon Photonic Biosensors with CMOS-Driven, Resonance-Tracking Readout. *APL Photonics* **2026**, *11*, 066109, doi:10.1063/5.0330876.
4. Alfaraj, N.; Helmy, A.S. Silicon-Integrated Next-Generation Plasmonic Devices for Energy-Efficient Semiconductor Applications. *Adv. Mater. Technol.* **2025**, *10*, e00389, doi:10.1002/admt.202500389.
5. Butt, M.A. Dielectric Waveguide-Based Sensors with Enhanced Evanescent Field: Unveiling the Dynamic Interaction with the Ambient Medium for Biosensing and Gas-Sensing Applications—A Review. *Photonics* **2024**, *11*, 198, doi:10.3390/photonics11030198.
6. Gao, Y.; Dong, P.; Shi, Y. Suspended Slotted Photonic Crystal Cavities for High-Sensitivity Refractive Index Sensing. *Opt. Express* **2020**, *28*, 12272–12278, doi:10.1364/OE.386678.
7. Butt, M.A.; Słowikowski, M.; Drecka, D.; Jarosik, M.; Piramidowicz, R. Experimental Characterization of a Silicon Nitride Asymmetric Loop-Terminated Mach-Zehnder Interferometer with a Refractive Index-Engineered Sensing Arm. *Nanomaterials* **2025**, *15*, 1532, doi:10.3390/nano15191532.
8. Bryan, M.R.; Butt, J.N.; Bucukovski, J.; Miller, B.L. Biosensing with Silicon Nitride Microring Resonators Integrated with an On-Chip Filter Bank Spectrometer. *ACS Sens.* **2023**, *8*, 739–747, doi:10.1021/acssensors.2c02276.
9. Bastos, A.R.; Vicente, C.M.S.; Oliveira-Silva, R.; Silva, N.J.O.; Tacão, M.; Costa, J.P. da; Lima, M.; André, P.S.; Ferreira, R.A.S. Integrated Optical Mach-Zehnder Interferometer Based on Organic-Inorganic Hybrids for Photonics-on-a-Chip Biosensing Applications. *Sensors* **2018**, *18*, 840, doi:10.3390/s18030840.
10. Dai, X.; Mihailov, S.J.; Blanchetiere, C. Ridge Waveguide Bragg Grating Pressure Sensor. In Proceedings of the Photonics North 2008; SPIE, August 12 2008; Vol. 7099, pp. 580–587.
11. Prasanna Kumaar, S.; Sivasubramanian, A. Analysis of BCB and SU 8 Photonic Waveguide in MZI Architecture for Point-of-Care Devices. *Sens. Int.* **2023**, *4*, 100207, doi:10.1016/j.sintl.2022.100207.
12. Saavedra, C.; Pandey, D.; Alt, W.; Meschede, D.; Pfeifer, H. Spectroscopic Gas Sensor Based on a Fiber Fabry-Perot Cavity. *Phys. Rev. Appl.* **2022**, *18*, 044039, doi:10.1103/PhysRevApplied.18.044039.
13. Sun, X.; Zhou, L.; Xie, J.; Zou, Z.; Lu, L.; Zhu, H.; Li, X.; Chen, J. Tunable Silicon Fabry–Perot Comb Filters Formed by Sagnac Loop Mirrors. *Opt. Lett.* **2013**, *38*, 567, doi:10.1364/OL.38.000567.
14. Pruessner, M.W.; Stievater, T.H.; Rabinovich, W.S. Integrated Waveguide Fabry-Perot Microcavities with Silicon/Air Bragg Mirrors. *Opt. Lett.* **2007**, *32*, 533, doi:10.1364/OL.32.000533.
15. Arianfard, H.; Wu, J.; Juodkazis, S.; Moss, D.J. Three Waveguide Coupled Sagnac Loop Reflectors for Advanced Spectral Engineering. *J. Light. Technol.* **2021**, *39*, 3478–3487, doi:10.1109/JLT.2021.3066256.

16. Arianfard, H.; Juodkazis, S.; Moss, D.J.; Wu, J. Sagnac Interference in Integrated Photonics. *Appl. Phys. Rev.* **2023**, *10*, 011309, doi:10.1063/5.0123236.
17. Butt, M.A.; Janaszek, B. A Coupled Resonator Optical Waveguide-Based Refractive Index Sensor Employing Sagnac Loop Reflectors. *Sensors* **2026**, *26*, 1448, doi:10.3390/s26051448.
18. Ngiejungbwen, L.A.; Hamdaoui, H.; Chen, M.-Y. Polymer Optical Fiber and Fiber Bragg Grating Sensors for Biomedical Engineering Applications: A Comprehensive Review. *Opt. Laser Technol.* **2024**, *170*, 110187, doi:10.1016/j.optlastec.2023.110187.
19. Amanti, F.; Andrini, G.; Armani, F.; Barbato, F.; Bellani, V.; Bonaiuto, V.; Cammarata, S.; Campostrini, M.; Dao, T.H.; De Matteis, F.; et al. Integrated Photonic Passive Building Blocks on Silicon-on-Insulator Platform. *Photonics* **2024**, *11*, 494, doi:10.3390/photonics11060494.
20. Vieu, C.; Carcenac, F.; Pépin, A.; Chen, Y.; Mejias, M.; Lebib, A.; Manin-Ferlazzo, L.; Couraud, L.; Launois, H. Electron Beam Lithography: Resolution Limits and Applications. *Appl. Surf. Sci.* **2000**, *164*, 111–117, doi:10.1016/S0169-4332(00)00352-4.
21. Huang, L.; Yan, H.; Xu, X.; Chakravarty, S.; Tang, N.; Tian, H.; Chen, R.T. Improving the Detection Limit for On-Chip Photonic Sensors Based on Subwavelength Grating Racetrack Resonators. *Opt. Express* **2017**, *25*, 10527–10535, doi:10.1364/OE.25.010527.
22. Lu, K.; Huang, B.; Lv, X.; Zhang, Z.; Ma, Z. Ultrasensitive Silicon Photonic Refractive Index Sensor Based on Hybrid Double Slot Subwavelength Grating Microring Resonator. *Sensors* **2024**, *24*, 1929, doi:10.3390/s24061929.
23. Talebi Khoshmehr, M.; Akca, B.I.; Słowikowski, M.; Dagmara, D.; Juchniewicz, M.; Piramidowicz, R.; Butt, M.A. Waveguide Geometry–Driven Trade-Offs in Resonant Cavity Sensor Performance. *Adv. Opt. Mater.* **2026**, e71376, doi:10.1002/adom.71376.
24. Curcio, J.A.; Petty, C.C. The Near Infrared Absorption Spectrum of Liquid Water. *J. Opt. Soc. Am.* **1951**, *41*, 302, doi:10.1364/JOSA.41.000302.
25. Dumon, P.; Bogaerts, W.; Wiaux, V.; Wouters, J.; Beckx, S.; Van Campenhout, J.; Taillaert, D.; Luyssaert, B.; Bienstman, P.; Van Thourhout, D.; et al. Low-Loss SOI Photonic Wires and Ring Resonators Fabricated With Deep UV Lithography. *IEEE Photonics Technol. Lett.* **2004**, *16*, 1328–1330, doi:10.1109/LPT.2004.826025.
26. Hale, G.M.; Querry, M.R. Optical Constants of Water in the 200-Nm to 200-Mm Wavelength Region. *Appl. Opt.* **1973**, *12*, 555, doi:10.1364/AO.12.000555.
27. Høvik, J.; Aksnes, A. A Study of Approximations for Accurate Two-Dimensional Simulations of Photonic Components. In Proceedings of the Advanced Photonics 2016 (IPR, NOMA, Sensors, Networks, SPPCom, SOF); OSA: Vancouver, 2016; p. JTu4A.7.
28. Gonzalo Wangüemert-Pérez, J.; Cheben, P.; Ortega-Moñux, A.; Alonso-Ramos, C.; Pérez-Galacho, D.; Halir, R.; Molina-Fernández, I.; Xu, D.-X.; Schmid, J.H. Evanescent Field Waveguide Sensing with Subwavelength Grating Structures in Silicon-on-Insulator. *Opt. Lett.* **2014**, *39*, 4442, doi:10.1364/OL.39.004442.
29. Janaszek, B.; Kieliszczyk, M.; Butt, M.A. Coherent Cavity Coupling in O-Band Silicon Photonic Sensors for Water Environment Detection. *Sci. Rep.* **2026**, doi:10.1038/s41598-026-53041-1.
30. Fewell, M.P.; Von Trojan, A. Absorption of Light by Water in the Region of High Transparency: Recommended Values for Photon-Transport Calculations. *Appl. Opt.* **2019**, *58*, 2408, doi:10.1364/AO.58.002408.
31. Balderas López, J.A.; Díaz-Reyes, J. Photopyroelectric Technique for the Measurement of Optical Properties of Pure Liquids. *Superf. Vacío* **2023**, *36*, 230801, doi:10.47566/2023_syv36_1-230801.
32. Butt, M.A.; Kozlowski, L.; Słowikowski, M.; Juchniewicz, M.; Drecka, D.; Filipiak, M.; Golas, M.; Stonio, B.; Dudek, M.; Piramidowicz, R. Investigation of Modal Characteristics

of Silicon Nitride Ridge Waveguides for Enhanced Refractive Index Sensing. *Micromachines* **2025**, *16*, 119, doi:10.3390/mi16020119.
33. Consani, C.; Dubois, F.; Auböck, G. Figures of Merit for Mid-IR Evanescent-Wave Absorption Sensors and Their Simulation by FEM Methods. *Opt. Express* **2021**, *29*, 9723, doi:10.1364/OE.415825.
34. Ardoino, N.; Lunelli, L.; Pucker, G.; Vanzetti, L.; Favaretto, R.; Pasquardini, L.; Pederzolli, C.; Guardiani, C.; Potrich, C. Optimization of Surface Functionalizations for Ring Resonator-Based Biosensors. *Sensors* **2024**, *24*, 3107, doi:10.3390/s24103107.
35. Butt, M.A.; Janaszek, B. A Coupled Resonator Optical Waveguide-Based Refractive Index Sensor Employing Sagnac Loop Reflectors. *Sensors* **2026**, *26*, 1448, doi:10.3390/s26051448.
36. Luan, E.; Yun, H.; Ma, M.; Ratner, D.M.; Cheung, K.C.; Chrostowski, L. Label-Free Biosensing with a Multi-Box Sub-Wavelength Phase-Shifted Bragg Grating Waveguide. *Biomed. Opt. Express* **2019**, *10*, 4825, doi:10.1364/BOE.10.004825.
37. Castelló-Pedrero, L.; Gómez-Gómez, M.I.; García-Rupérez, J.; Griol, A.; Martínez, A. Performance Improvement of a Silicon Nitride Ring Resonator Biosensor Operated in the TM Mode at 1310 Nm. *Biomed. Opt. Express* **2021**, *12*, 7244, doi:10.1364/BOE.437823.
38. Janaszek, B.; Kieliszczyk, M.; Butt, M.A. Coherent Cavity Coupling in O-Band Silicon Photonic Sensors for Water Environment Detection. *Sci. Rep.* **2026**, *16*, 22640, doi:10.1038/s41598-026-53041-1.
39. Xu, P.; Yao, K.; Zheng, J.; Guan, X.; Shi, Y. Slotted Photonic Crystal Nanobeam Cavity with Parabolic Modulated Width Stack for Refractive Index Sensing. *Opt. Express* **2013**, *21*, 26908, doi:10.1364/OE.21.026908.
40. Ciminelli, C.; Dell'Olio, F.; Conteduca, D.; Campanella, C.M.; Armenise, M.N. High Performance SOI Microring Resonator for Biochemical Sensing. *Opt. Laser Technol.* **2014**, *59*, 60–67, doi:10.1016/j.optlastec.2013.12.011.
41. Yao, K.; Shi, Y. High-Q Width Modulated Photonic Crystal Stack Mode-Gap Cavity and Its Application to Refractive Index Sensing. *Opt. Express* **2012**, *20*, 27039, doi:10.1364/OE.20.027039.
42. Chow, E.; Grot, A.; Mirkarimi, L.W.; Sigalas, M.; Girolami, G. Ultracompact Biochemical Sensor Built with Two-Dimensional Photonic Crystal Microcavity. *Opt. Lett.* **2004**, *29*, 1093, doi:10.1364/OL.29.001093.